Visualization of myosin II filament dynamics in remodeling acto-myosin networks with interferometric scattering microscopy

Lewis S. Mosby[1,2]*, Nikolas Hundt[3,⊡,]*, Gavin Young[3], Adam Fineberg[3], Marco Polin[1,2], Satyajit Mayor[4,5,#], Philipp Kukura[3#], Darius V. Köster[1,6#]

1 Centre for Mechanochemical Cell Biology, University of Warwick, Coventry CV4 7AL, UK

2 Physics Department, University of Warwick, Coventry CV4 7AL, UK

3 Physical and Theoretical Chemistry Laboratory, Department of Chemistry, University of Oxford, South Parks Road, Oxford OX1 3QZ, UK

4 National Centre for Biological Sciences, Tata Institute for Fundamental Research, GKVK, Bellary Road, Bangalore 560065, India

5 Institute for Stem Cell Biology and Regenerative Medicine, Bangalore 560065, India

6 Division of Biomedical Sciences, Warwick Medical School, University of Warwick, Coventry CV4 7AL, UK

* equal contribution

#corresponding authors: philipp.kukura@chem.ox.ac.uk, d.koester@warwick.ac.uk, mayor@ncbs.res.in

⊡ current address: Department of Cellular Physiology, Biomedical Center, Ludwig-Maximilians-Universität München, Großhaderner Str. 9, 82152 Planegg/Martinsried, Germany

Abstract

The plasma membrane and the underlying cytoskeletal cortex constitute active platforms for a variety of cellular processes. Recent work has shown that the remodeling acto-myosin network modifies local membrane organization, but the molecular details are only partly understood due to difficulties with experimentally accessing the relevant time and length scales. Here, we use interferometric scattering (iSCAT) microscopy to investigate a minimal acto-myosin network linked to a supported lipid bilayer membrane. Using the magnitude of the interferometric contrast, which is proportional to molecular mass, and fast acquisition rates we detect and image individual membrane attached actin filaments diffusing within the acto-myosin network and follow individual myosin II filament dynamics. We quantify

myosin II filament dwell times and processivity as a function of ATP concentration, providing evidence for the predicted ensemble behavior of myosin head domains. Our results show how decreasing ATP concentrations lead to both increasing dwell times of individual myosin II filaments and a global change from a remodeling to a contractile state of the acto-myosin network.

Introduction

The acto-myosin cortex is critical for the mechanical stability of the cell and the organization of the adjacent plasma membrane. Several studies have shown that the cell cortex affects the dynamics and mobility of membrane components (1–3) and there is increasing evidence that dynamic remodeling of the acto-myosin network drives local flow and clustering of membrane molecules (4–7). The complexity of the acto-myosin cortex and plasma membrane in live cells, however, makes it difficult to study the molecular details of cortex-membrane interactions and to uncover the underlying mechanisms. Reconstituted minimal systems, where fluorescently labeled proteins are visualized using confocal or total internal reflection fluorescence (TIRF) microscopy, provide a tractable way to study the dynamics of two-dimensional, membrane-bound acto-myosin networks (8–11). These systems can adopt a range of active states depending on ATP concentration, actin to myosin ratio, actin filament length distribution and concentration (10, 11). Despite extensive theoretical and experimental analysis on the molecular and macroscopic level, the processes that lead from a remodeling, fluid-like acto-myosin network at high ATP concentrations to a contractile, solid-like network at low ATP concentrations remain poorly understood.

Most experimental and theoretical studies of myosin motor properties rely on experiments with single motor head domains. Recent advances in the theoretical understanding of myosin II filaments formed of multiple head domains indicate that small changes in the single-head duty ratio can lead to a switch from non-processive to processive behavior due to cooperative effects (12–15). To experimentally test the

dynamics and properties of multi-headed myosin II filaments, it is necessary to visualize the network components with a sub-second time-resolution over timescales of tens of minutes, which has been challenging to achieve with fluorescent probes due to photo-bleaching and photo-toxicity.

Here, we employed interferometric scattering (iSCAT) microscopy (16, 17), a label-free imaging technique that relies on the interference between reflected and scattered light from nano-objects near an interface. The key advantages of light scattering over fluorescence detection in this context are the lack of an upper limit to fluorescence emission rate and the absence of photobleaching and thus photobleaching, enabling long observation times at high acquisition rates (> 1kHz). We quantify microscopic quantities, such as actin filament diffusion rates, myosin filament dwell times and processivity, while simultaneously monitoring mesoscopic phenomena such as network flows and clustering. This allows us to link changes in the mechanochemical properties of myosin II filaments to transitions in the acto-myosin network, namely from the remodeling to the contractile state.

Results

Detection and characterization of actin and myosin filaments

The critical step to use label-free imaging to the study of acto-myosin dynamics on a membrane requires detection and distinguishing actin from myosin II filaments. Due to the absence of crowding factors or excess proteins in our experiments, the actin and myosin II filaments were the principal sources of light scattering after subtraction of background signatures originating from cover glass roughness (Fig. 1A, Fig. S1A) (see methods). Actin and myosin II filaments landing on bare glass slides exhibited contrasts of -0.058 ± 0.015 and -0.12 ± 0.013, respectively (Fig. 1B-D). This difference in interferometric contrasts reflects the lower mass of actin compared to myosin II filaments per unit length ($m_{F\text{-}actin}$ / m_{myoII} = 0.42) (18–20) and the scaling of the interferometric signal with molecular mass (21). Myosin II filaments

exhibited an apparent average length of 520 ± 130 nm (N=269) (Fig. S1B) as reported earlier (10). The clear difference in interferometric contrast and the characteristic, uniform shape of myosin II filaments provided a good basis to distinguish them reliably from actin filaments.

Turning to supported lipid bilayers (SLB), we characterized the formation of actin networks. After directly observing successful SLB formation (Video 1), incubation with an actin-membrane linking protein (deca-histidine tagged Ezrin-actin binding domain) (22) and addition of actin filaments (see methods), we observed, that the SLB did not alter the contrast of actin filaments and that regions exhibiting consecutive deposition of multiple actin filaments within a diffraction-limited spot displayed a step-wise increase in the interferometric signal (Fig. S1C-D; Video 2). Based on the local contrast, we estimated that, under the conditions used here ([G-actin] = 100-350 nM), the actin layers are 1 to 6 filaments thick, with 2 filaments per diffraction-limited spot being most frequent (Fig. S1E). Evaporation was below 5% during a period of 60 minutes, so that salt and protein concentrations can be considered to be constant over the time course of a typical experiment (Fig. S1F)

The mobility of actin filaments depends strongly on the number of tethering points to the SLB and on its fluidity. As a result, actin filaments longer than 5 µm are essentially static in the absence of external forces (e.g. by myosin motors), whereas short actin filaments exhibited higher mobility (23) (see supplementary information). Offline background subtraction to remove static actin network components revealed the mobile filament fraction, with free diffusion for actin filaments shorter than 1.5 µm (Fig. 1E, F; S1G, Video 3) and confined diffusion for filaments longer than 1.5 µm (Fig. 1G-H, S1H, Video 4). To compare the mobility of different actin filaments, we measured the slope of the mean-squared displacement over time for time-intervals longer than 5s. The reduced mobility of longer filaments especially in their displacement perpendicular to the filament orientation (see Fig. 1G, $MSD_{\perp}$) indicates confinement by static components of the actin network and is typical for reptation of a flexible polymer within a meshwork in 2D (24).

Binding dynamics of myosin II filaments to actin

We then characterized myosin II filament binding to membrane-bound actin networks at 100 µM ATP (t= 1 min), which fuels continuous network remodeling, and at t = 16 min, when ATP concentration dropped below 10 µM ATP leading to network contraction, as described previously (11, 25, 26) (Fig. S2A, B; Video 5). It is to note, that the change in network contractility was due to changes in the available ATP, and addition of fresh ATP could reverse the strong binding of myosin II filaments (Video 6). By creating kymographs along the tracks of myosin II filaments (Fig. S2C, D; Video 7), we found that the distribution of myosin II dwell times on F-actin followed a double-exponential decay function. At t = 1 min, the computed time constants were τ_{off1} = 1.23 s ([1.36 s - 1.12 s]$_{95\%}$) and τ_{off2} = 12.6 s ([14 s - 11.3 s]$_{95\%}$) with 66% - 71% of the events being described by τ_{off1} (Fig. 2A). At t = 16 min, the myosin II filament dwell time constants were τ_{off1} = 3.7 s ([3.1 s - 4.2 s]$_{95\%}$) and τ_{off2} = 11.9 s ([9.4 s - 15.5 s]$_{95\%}$) with 63 % - 87 % of the events being described by τ_{off1} (Fig. 2B). The observation that the dwell time distributions seem to follow a double exponential function might be due to the separate or simultaneous binding of the two ends of myosin filaments to actin (see discussion)(28).

We went on to analyze the motion of myosin II filaments. At t = 1min, the mobile myosin II filaments exhibited a velocity distribution that can be described by a sum of two Gaussians with >60 % of myosin II filaments travelling at $v_{myoII,1}$ = 0.04 (±0.03) µm s^{-1} and the remaining at $v_{myoII,2}$ = 0.20 (±0.13) µm s^{-1} (Fig. 2C). The corresponding run length distribution decays exponentially with a characteristic run length of λ = 0.23 (±0.03) µm (Fig. 2D). Plotting run length versus dwell time (i.e. total time of attachment during which the run happened) shows a moderate positive correlation (Pearson coefficient 0.38) for dwell times < 3 s and a weak negative correlation (Pearson coefficient -0.17) for longer binding times (Fig. 2E, Fig. S2E). This implies that the population corresponding to short dwell times is mobile while the population with long dwell times exhibits slow, reduced motion and eventually becomes immobilized.

At t = 16 min, mobile myosin II filaments travelled with an average velocity of v_{myoII} = 0.46 (±0.20) µm s^{-1} (Fig. 2F, single Gaussian distribution) and the characteristic run length is λ = 1.03 (±0.05) µm (Fig. 2G). The correlation between run length and dwell time is stronger compared to t = 1 min with most myosin II filaments exhibiting persistent motion for up to 6 s (Pearson coefficient 0.57) and a loss of this correlation at longer dwell times (Pearson coefficient -0.18) (Fig. 2H, Fig. S2F).

To assess whether the measured velocities were a combination of myosin and actin network motion, we applied a 50 frames median filter (corresponding to 10s) filtering out the fast-moving myosin II filaments and highlighting actin filament motion. The largest actin network displacements that we could observe occurred only locally and sporadically and did not exceed 50 nm s^{-1} in the contractile state (t = 16 min) and 15 nm s^{-1} in the remodeling state at t = 1 min (Fig. S2G). These observations are in agreement with earlier studies (8, 11) and underline that myosin II filament velocities result directly from motor activity on actin.

Myosin II filament tracking reveals links between binding mode, orientation and mobility

Given the characteristic shape of myosin filaments and the signal-to-noise ratio achievable with iSCAT microscopy, we performed single-particle tracking (SPT) to corroborate the above measurements and to analyze the dynamics of individual myosin II filaments as a function of time. By analyzing the intensity distribution of pixels belonging to each myosin II filament, we could extract the particle location and orientation for each time point. Tracks were generated based on criteria including the particle size and the maximum step size between frames (see supplementary text for details of the SPT routine). In addition, quantifying the MSD of particles and computing the correlation in displacements between adjacent timesteps, individual myosin II filament tracks could be divided into periods of diffusive and processive motion (Fig. S3A-E, Video 8). We used the average MSD and correlation data at t = 1 min (100 µM ATP) as a threshold to classify individual tracks. The motion we classify as diffusive most likely

represents a weakly interacting state of myosin II filaments with actin filaments with increased angular orientation fluctuations and little displacement, as fully detached myosin II filaments would escape the imaging plane rapidly.

This automated detection method provided a more comprehensive picture of myosin II filament dynamics in the remodeling state at t = 1 min (100 µM ATP) and at the contractile state (t = 16 min) (Fig. 3A, B) as well as increased the sensitivity for short binding. At t = 1 min (100 µM ATP), we found characteristic binding times of τ_{off1} = 0.34 s (0.33 s- 0.35 s), τ_{off2} = 2.26 s (2.13 s - 2.41 s) and τ_{off3} = 10.9 s (9 s – 12.8 s) and at t = 16 min τ_{off1} = 0.41 s (0.39 s - 0.43 s), τ_{off2} = 2.46 s (2.33 s - 2.63 s) and τ_{off3} = 11 s (10 s – 12.5 s) (Fig. 3C). As observed above, the characteristic binding times were slightly longer, and the number of events with binding times longer than 3 s increased 1.6-fold and more when comparing the remodeling state to the contractile state (Fig. S3F). The increase in long duration binding events in the contractile state could be an underestimate as only binding-unbinding cycles occurring within the recording time were considered and myosin II filaments traveling into clusters or out of the field of view were discarded.

Interestingly, we observed a larger increase in the fraction of processively moving myosin II (N_{proc}/N = 221/35644 at t = 1 min; N_{proc}/N = 640/35358 at t = 16 min). Concomitantly, analyzing individual tracks of myosin II filaments revealed that the fraction of total bound time spent performing processive motion increased from 0.3 (±0.2) at t = 1 min to 0.5 (±0.3) at t = 16 min (Fig. 3D, S3G). These results indicate that the contractile state is driven by both an increased total number of processively moving myosin II filaments and a higher persistence of each myosin II filament. To assess, whether the properties of individual myosin motors changed during the course of the experiment, we analyzed the step size distribution of all recorded tracks. However, there were no detectable changes over the course of the transition from remodeling to contractile state (Fig. S3H). By computing the angle α between myosin II filament orientation and its velocity direction for each myosin II filament step, we found that α varied

significantly (± 45° FWHM) at t = 1 min, whereas it narrowed with increasing time to ±25° (FWHM) at t = 16 min (Fig. 3E, S3I). Importantly, at t = 16 min, the majority of processively moving myosin II filaments are aligned with their direction of propagation (Fig. 3F, S3J). This indicates that the increased processivity is not linked to changes in the step size or rate of myosin II filaments but is due to improved alignment with the actin tracks supporting long range transport and buildup of persistent material flows and directed forces that can drive network contraction. A decrease in α at t = 16 min could be due to higher numbers of myosin head domains binding to actin filaments, however, the high rotational flexibility of individual head domains provides enough flexibility to allow the myosin filament to connect multiple actin filaments important to generate network contraction. We only considered tracks of myosin II filaments that were moving individually and that any events including the merging of multiple myosin II filaments or moving of myosin II filaments into clusters were disregarded which might result in a slight underestimation of the number of processive myosin II filaments.

Myosin II filament flows generate transiently stable contractile zones

In acto-myosin networks that reached their contracted state, we observed the formation of contractile zones, into which myosin II filaments moved continuously from multiple directions. These contractile zones were characterized by a cluster of myosin II filaments in their center holding multiple actin filaments together. Interestingly, despite the steady flow of myosin II filaments into the clusters, they did not seem to grow significantly. After subtracting the median image of the image sequence showing a cluster region, it became evident that myosin II filaments detached once they reached the core of the cluster preventing overall growth of the myosin II filament cluster (Fig. 4A, B; Video 9). This could be due to the lack of free actin filaments and mechanical tension inside the clusters forcing excess myosin filaments to leave the zone.

Simulations indicate a connection between increased fraction of myosin II filaments with long attachment times and the transition to a contractile network state

To test whether the observed changes in myosin II filament fractions with longer dwell times are indeed driving the acto-myosin network contraction, we ran simulations using Cytosim (cytosim.org), an open source simulation engine that models acto-myosin network dynamics based on Brownian dynamics (29). Following published simulation templates (30), actin filaments were represented by a set of equidistant points with a characteristic bending rigidity of 7.3 10^{-26} Nm^2 (31) and myosin II filaments by two motor domains connected by a short, stiff rod (50 nm, 300 Nm/rad rotational stiffness). The motors followed a linear force-speed dependency (30) and two types of motors were introduced to match our experimental observations (Cytosim cannot model multiheaded muscular myosin II filaments): type 1 with a short binding time $\tau_{off,\,1}$ = 2.4 s, $v_{max,\,1}$ = 200 nm s^{-1} and $F_{max,\,1}$ = 6 pN and type 2 with $\tau_{off,\,2}$ = 10.9 s, $v_{max,\,2}$ = 50 nm s^{-1} and $F_{max,\,2}$ = 6 pN . Simulations were computed for a circular field of 12 µm radius containing 400 actin filaments of 4 µm length and a combination of type 1 and type 2 motors reflecting the experimental conditions in terms of actin filament and motor protein density. Starting with 1200 type 1 motors and increasing the number of type 2 motors, we found that the network shifted from a remodeling to a more contractile state when the ratio of type 2 to type 1 motors reached 1:20 or higher (Fig. 4C, Video 10, 11). Using higher numbers of type 2 motors accelerates the contraction process, which implies that the long binding motors are better crosslinkers than the short binding motors. To test, whether this effect was simply due to the increase in motors, we ran the simulations with 1500 type 1 motors and 0, 50 or 80 type 2 motors and did not observe network contraction with type 1 motors only but observed again a clear tendency to clustering at motor ratios above 20:1 (Fig. S4A, Video 12). The simulations were in agreement with our experimental observations of actomyosin networks first displaying remodeling behavior followed by contractions into multiple small asters converging finally into one cluster (Video 5). Taken together, this suggests that the dual behavior of myosin II filaments acting

as motors and crosslinkers is important to drive clustering of acto-myosin networks and that crossing a critical threshold of a relatively small number of long binding, cross-linking myosin II filaments mediates the transition from the remodeling to the contractile state (Fig. 4D).

Discussion

Studying myosin II filament dynamics inside a membrane-bound, dynamic actin network provides insights on how mesoscale network dynamics are related to minute changes of the physico-chemical properties of motor head domains in myosin II filaments. Our approach demonstrates that a change in myosin II filament dwell times is related to a change of the acto-myosin network from a remodeling to a contractile state. This is underlined by the observation that myosin II filaments move faster and more processively in the contractile state than in the remodeling state at 100 µM ATP. Myosin II filaments can be under mechanical load depending on the actin network organization and our observations of myosin II filament dynamics corroborate predictions made by theoretical studies (15, 32).

Given the large number of myosin head domains within a single myosin II filament, we would expect complex binding behavior with multiple characteristic attachment times. Our data, however, shows that myosin II filament binding is determined by 3 major time scales: τ_{off0} in the range of 0.3-0.4 s, τ_{off1} in the 2-3 s range and τ_{off2} in the 10 s range. The shortest time scale likely corresponds to the binding - unbinding of a single myosin head domain (33). Considering the dumbbell structure of myosin II filaments, we attribute τ_{off1} to the binding of myosin head domains at one side of the dumbbell, whereas τ_{off2} would represent the simultaneous binding of myosin heads from both sides. This model explains the behavior of myosin filaments at low [ATP] concentrations, where they are better aligned along the direction of processive motion. As the trailing end of a myosin filament wanders off axis less than at high [ATP], it is less likely to encounter another actin filament and form a crosslink. Therefore, at low ATP concentrations, we observe a reduction of long dwells with short run lengths. Once the myosin filaments

reach the plus end of an actin filament, however, the increased processivity will contribute to the condensation of actin filaments by the motors' free end catching and pulling adjacent actin filaments. This promotes the formation of contractile zones in more crowded regions of the actin filament network. The effect of myosin II filaments cross-bridging multiple actin filaments on network contractility and entropy production was also reported by the Murrell group (34).

The large temporal dynamic range of iSCAT microscopy allowed us to reveal the dynamics within acto-myosin clusters. Interestingly, at low but not limiting ATP concentrations, myosin II filaments continuously moved into the clusters, probably detaching upon reaching the clusters' center. From single-molecule studies on different myosin isoforms it is known that mechanical load increases the dwell times of myosin heads on actin filaments (35, 36). For processive motor ensembles such as myosin II filaments it was predicted that this would lead to increased run lengths on actin (15, 32). Due to acto-myosin network dynamics and contraction of actin filaments into asters, myosin filaments that crosslink actin filaments between two asters might experience high mechanical load, which increases their dwell times and promotes processive motion. Once a myosin II filament reaches the center of a cluster, however, it will experience a sudden drop in mechanical load due to a lack of available actin filaments for interfilament crosslinks leading to detachment. This intrinsic mechano-regulation may contribute in the formation of constituently contractile zones, which could drive the clustering of actin-binding membrane proteins as observed in cells (4). A detailed comparison of our data with theoretical models (15, 32) is in preparation. This will further our understanding of the molecular mechanisms that lead to extended dwell times as well as the effect of mechanical load at different ATP concentrations.

Together with the Cytosim based simulations, our experimental observations indicate that a combination of motors with different dwell times, promoting different modes of myosin interaction with the actin network, could provide a simple and biologically feasible strategy for a biological system to switch between a remodeling (fluid-like) and a contractile (solid-like) state. Short dwell times of myosin

filaments limit the interaction with actin filaments leading to weak interaction and lack of persistent motion with little effect on the actin network. Intermediate binding times lead to processive motion along single actin filaments at high velocities, generating advective flows of myosin filaments, but with only occasional binding to other actin filaments and hence only local remodeling of the actin network. In contrast, long dwell times increase the chance of myosin filaments to crosslink multiple actin filaments, rendering myosin filaments immobile, but causing large-scale network contractions and actin filament flows through persistent motor action (Fig. 4D). The importance of the control of network crosslinking as a way to change network contractility can be understood in terms of percolation theory (37), and its relevance for the understanding of diseases was for example shown for the actin crosslinker α-actinin (38).

Materials and Methods

Purified Proteins

Actin was purified from chicken breast following the protocol from Spudich and Watt (39) and kept on ice in monomeric form in G-buffer (2 mM Tris Base, 0.2 mM ATP, 0.5 mM TCEP-HCl, 0.04% NaN_3, 0.1 mM CaCl2, pH 7.0) (11). The experiments using iSCAT microscopy were performed with myosin II obtained from chicken breast following a modified protocol from Pollard (40) and kept in monomeric form in myo-buffer (500 mM KCl, 1 mM EDTA, 1 mM DTT, 10 mM HEPES, pH 7.0). The day prior to experiments, functional myosin II proteins were separated from proteins containing dead head domains by a round of binding and unbinding to F-actin at a 5:1 actin to myosin ratio (switch from no ATP to 3 mM ATP) followed by a spin at 60,000 rpm for 10 min at 4 ^{o}C in a TLA100.3 rotor. The supernatant containing functional myosin II is dialyzed against myo-buffer overnight and used for experiments for up to three days.

To control the length of actin filaments, we titrated purified murine capping protein to the actin polymerization mix. The purification of capping protein was described earlier (11). To link actin to the SLB, we used a construct containing 10x His domains followed by a linker (KCK) and the actin binding domain of Ezrin (HKE) as described earlier (11).

Supported Lipid Bilayer and Experimental Chamber Preparation

Glass coverslips (#1.5 borosilicate, Menzel, Germany) for SLB formation were cleaned with Hellmanex III (Hellma Analytics, Mühlheim, Germany) following the manufacturer's instructions followed by thorough rinses with EtOH and MilliQ water, blow dried with N_2 and finally passed briefly over a Bunsen burner flame. For the experimental chamber, 0.2 ml PCR tubes (Tarsons Products, Kolkata, India) were cut to remove the lid and conical bottom part. The remaining ring was stuck to the cleaned glass using UV glue (NOA88, Norland Products, Cranbury, NJ) and three minutes curing by intense UV light at 365 nm (PSD-UV8T, Novascan, Ames, IA). Freshly cleaned and assembled chambers were directly used for experiments.

Supported lipid bilayers (SLB) containing 98% DOPC and 2% DGS-NTA(Ni^{2+}) lipids were formed by fusion of small uni-lamellar vesicles (SUV) as described earlier (11). Prior to experiments with F-actin we formed SLBs in chambers filled with 100 µl KMEH (50 mM KCl, 2 mM $MgCl_2$, 1 mM EGTA, 20 mM HEPES, pH 7.2). SLB formation was observed live using ISCAT microscopy, to ensure that sufficient SUVs fused to form a uniform, fluid lipid bilayer without holes (Video 1).

Formation of Acto-Myosin Network

In a typical experiment, SLBs were formed, incubated with 10 nM HKE for 40 min and washed three times with KMEH. During this incubation time, F-actin was polymerized. First $10\%_{vol}$ of 10x ME buffer

(100 mM MgCl2, 20 mM EGTA, pH 7.2) were mixed with the G-actin stock and incubated for 2 min to replace G-actin bound Ca^{2+} ions with Mg^{2+}. Addition of 2x KMEH buffer supplemented with 2 mM Mg-ATP induced F-actin polymerization at a final G-actin concentration of 5 µM. After 20-30 min incubation, the desired amount of F-actin was added to the SLBs using blunt-cut 200 µl pipette tips. An incubation of 30 min allowed the F-actin layer to reach an equilibrium state of binding to the SLB. For the addition of myosin II filaments to the sample, intermediate dilutions of myosin II proteins were prepared in milliQ water at 10 times the final concentration from fresh myosin II stock (4 mM, 500mM KCl) in a test tube and incubated for 5 min to allow the myosin II filament formation. Then, 1/10 of the sample buffer was replaced with the myosin II filament solution and supplemented with Mg-ATP (100 mM) at 0.1 mM final concentration. Afterwards, the dynamics of the acto-myosin system were observed for up to 60 min. The system usually showed a remodeling behavior for the first 10-15 min before contraction and aster formation started (due to ATP concentrations below 10 µM as estimated from the activity of myosin II and earlier reports (25)). Once, the system reached a static, jammed state and no myosin activity could be observed, the system could be reset into a remodeling state by addition of Mg-ATP (100 mM) to a final concentration of 0.1 mM (Video 10). Each step of this procedure was performed on the microscope stage, which allowed us to check its state continuously. The open chamber design allowed the addition of each component from the top without induction of flows that would perturb the actin network. All experiments were performed at room temperature (22° C

Details about the actin, myosin and ATP concentrations used in each experiment can be found in table (S1).

iSCAT microscopes

Interferometric scattering microscopy was performed on two different home-built setups similar to those detailed in (41, 42). Briefly, a weakly focused laser beam was scanned across the sample over an

area of 24 x 24 μm^2 (445 nm laser) or 32.6 x 32.6 μm^2 (635 nm laser). The light reflected from the glass-water interface together with the scattered light from the sample was imaged onto a CMOS camera (445 nm laser: Point Grey GS3-U3-23S6M-C, Flir, Canada; 635 nm laser: MV-D1024-160-CL-8, Photonfocus, Switzerland). The cameras were controlled using home-written LabVIEW software. The setup with the 445 nm laser had a 3.5 mm partially reflective mirror placed in the re-imaged back focal plane of the objective for enhanced scattering contrast as described in (42). The videos were recorded at 50 fps (445 nm laser) and 25 fps (635 nm laser), and pre-averaged by a factor of 5 to reduce noise. The illumination intensity on the sample (445 nm laser: 250 W/cm^2; 635 nm laser: 1.9 kW/cm^2) was set to nearly saturate the camera with the returning light. The pixel sizes were 23.4 nm/pixel (445 nm laser) and 31.8 nm/pixel (635 nm laser).

Image processing

Non-sample specific illumination inhomogeneities, fixed-pattern noise and constant background were removed from the raw images by dividing each of them with a flat field image that contained only these features. The flat field image was computed by recording 2000 frames of the sample while moving the stage. For each pixel, a temporal median was calculated resulting in a flat field image that only contained static features.

Median filtering

Movies were median filtered using MATLAB (MathWorks, Natick, MA, USA). For each image sequence, the median is computed for each pixel, subtracted from the original image sequence and the median filtered image sequence as well as the computed median filter are saved.

Actin filament tracking

Actin filaments that became visible after median filtering and that did not cross other actin filaments for at least 1000 frames were tracked using image J (http://imagej.nih.gov) and the plugin JFilament (43, 44). The obtained tracking traces were analyzed using MATLAB to compute the position of the center of mass (CM) and the filament orientation for each time point and to generate plots of the CMs total mean square displacement as well as the parallel and perpendicular components of the mean square displacement with respect to the filament orientation.

Actin filament length measurements

Image stacks of actin filaments landing on the HKE decorated SLBs were taken at 10 Hz immediately after addition of actin filaments to the sample. Theses image stacks were split in segments of 10 s and the median of each segment was subtracted from its last frame, to visualize freshly landed, isolated actin filaments. The images were then converted from the 32-bit interferometric contrast values to 8-bit (by the formula $f(x) = 1000*(-x) + 1000$), bandpass filtered (low pass: 3 pixel, high pass: 20 pixel) and analyzed with the image J plugin Neuron J (45). Images of fluorescent actin filaments landing on HSE decorated SLBs shortly after their addition to the sample were directly converted to 8-bit and analyzed with Neuron J

Myosin II filament length measurements

Intensity line-scans along the long axis of single myosin filaments were taken and the distance between the half maximum points at both ends were taken as the length of the myosin II filament.

Myosin binding dynamics

Imaging with 5-10 Hz for several minutes was sufficient to capture a broad range of myosin filament dynamics with high accuracy. To remove any signal originating from static structures such as immobile actin filaments or small impurities in the SLB, the image sequences were median filtered (46). In a second step, a maximum projection of the time series was used to visualize the tracks occupied by myosin II filaments during the experiment. Lines following these tracks were then used to compute kymographs depicting the myosin II filament binding times and their motion along actin filaments (kymograph tool in Image J, line width 3). Dwell time, run length and velocity distributions were plotted and further analyzed using OriginPro 2018 (OriginLab Corporation, Northampton, MA, USA) and MATLAB. Best fitting functions for the myosin II filament dwell times were selected using MEMLET, which estimates the maximum likelihood of a fitting function to describe a data point distribution (47).

Detection and Tracking

Image analysis and single particle tracking (SPT) was carried out using ImageJ and Python code developed for this work (more detailed descriptions of the computational methods are provided in the Supplementary Information, code is available upon request).

Contributions:

DK conceived, designed and performed experiments, purified proteins, analyzed data, wrote manuscript; NH helped in the experiments, analyzed data, wrote manuscript; LM wrote the tracking code and performed analysis; GY and AF built the iSCAT microscopes; MP reviewed manuscript, advised in the development of the tracking code, reviewed/edited manuscript; PK conceived experiments, reviewed/edited manuscript; SM conceived experiments, reviewed/edited manuscript.

Acknowledgements

DK thanks Madan Rao (NCBS) and Kabir Husain (University of Chicago) for instructive discussions and comments on the manuscript, Mohan Balasubramanian (Warwick Medical School) for material support and instructive discussions, and the Company of Biologists for supporting this work with a Travelling fellowship. NH thanks James Sellers and Yasuharu Takagi from the NIH for providing the actin. DK was funded as a Campus Fellow at NCBS, later as a postdoctoral fellow in the Balasubramanian lab by ERC-2014-ADG N° 671083 and then as an assistant professor in the Wellcome-Warwick Quantitative Biomedical Program. NH was supported by DFG research fellowship, grant HU 2462/1-1, and later by a DFG return grant HU 2462/3-1. LM was supported by Leverhulme Trust Grant RPG-2016-260. GY was supported by a Zvi and Ofra Meitar Magdalen Graduate Scholarship; PK was supported by an ERC Starting Investigator Grant (Nanoscope, 337577). SM and this work were supported by a JC Bose Fellowship from the Department of Science and Technology, and a Margadarshi Fellowship IA/M/15/1/502018 (Wellcome Trust–Department of Biotechnology, India Alliance), from the Government of India.

References:

1. Kusumi, A., C. Nakada, K. Ritchie, K. Murase, K. Suzuki, H. Murakoshi, R.S. Kasai, J. Kondo, T. Fujiwara, and HidejiMurakoshi. 2005. Paradigm shift of the plasma membrane concept from the two-dimensional continuum fluid to the partitioned fluid: high-speed single-molecule tracking of membrane molecules. Annu. Rev. Biophys. Biomol. Struct. 34: 351–78.

2. Arumugam, S., and P. Bassereau. 2015. Membrane nanodomains: contribution of curvature and interaction with proteins and cytoskeleton. Essays Biochem. 57: 109–19.

3. Saka, S.K., A. Honigmann, C. Eggeling, S.W. Hell, T. Lang, and S.O. Rizzoli. 2014. Multi-protein

assemblies underlie the mesoscale organization of the plasma membrane. Nat. Commun. 5: 1–14.

4. Rao, M., and S. Mayor. 2014. Active organization of membrane constituents in living cells. Curr. Opin. Cell Biol. 29C: 126–132.

5. van Zanten, T.S., A. Cambi, M. Koopman, B. Joosten, C.G. Figdor, M.F. Garcia-Parajo, and T.S. Van Zanten. 2009. Hotspots of GPI-anchored proteins and integrin nanoclusters function as nucleation sites for cell adhesion. Proc. Natl. Acad. Sci. U. S. A. 106: 18557–62.

6. Plowman, S.J., C. Muncke, R.G. Parton, and J.F. Hancock. 2005. H-ras, K-ras, and inner plasma membrane raft proteins operate in nanoclusters with differential dependence on the actin cytoskeleton. Proc. Natl. Acad. Sci. U. S. A. 102: 15500–5.

7. Köster, D. V, and S. Mayor. 2016. Cortical actin and the plasma membrane: inextricably intertwined. Curr. Opin. Cell Biol. 38: 81–89.

8. Murrell, M.P., and M.L. Gardel. 2012. F-actin buckling coordinates contractility and severing in a biomimetic actomyosin cortex. Proc. Natl. Acad. Sci. U. S. A. .

9. Vogel, S.K., F. Heinemann, G. Chwastek, and P. Schwille. 2013. The design of MACs (minimal actin cortices). Cytoskeleton. 70: 706–717.

10. Ideses, Y., A. Sonn-Segev, Y. Roichman, and A. Bernheim-Groswasser. 2013. Myosin II does it all: assembly, remodeling, and disassembly of actin networks are governed by myosin II activity. Soft Matter. 9: 7127.

11. Köster, D.V., K. Husain, E. Iljazi, A. Bhat, P. Bieling, R.D. Mullins, M. Rao, and S. Mayor. 2016. Actomyosin dynamics drive local membrane component organization in an in vitro active composite layer. Proc. Natl. Acad. Sci. 113: E1645–E1654.

12. Bidone, T.C., W. Jung, D. Maruri, C. Borau, R.D. Kamm, and T. Kim. 2017. Morphological

Transformation and Force Generation of Active Cytoskeletal Networks. PLoS Comput. Biol. 13: e1005277.

13. Albert, P.J., T. Erdmann, and U.S. Schwarz. 2014. Stochastic dynamics and mechanosensitivity of myosin II minifilaments. New J. Phys. 16.

14. Rastogi, K., M.S. Puliyakodan, V. Pandey, S. Nath, and R. Elangovan. 2016. Maximum limit to the number of myosin II motors participating in processive sliding of actin. Sci. Rep. 6: 32043.

15. Erdmann, T., K. Bartelheimer, and U.S. Schwarz. 2016. Sensitivity of small myosin II ensembles from different isoforms to mechanical load and ATP concentration. Phys. Rev. E. 94: 1–9.

16. Kukura, P., H. Ewers, C. Müller, A. Renn, A. Helenius, and V. Sandoghdar. 2009. High-speed nanoscopic tracking of the position and orientation of a single virus. Nat. Methods. 6: 923–927.

17. Young, G., and P. Kukura. 2019. Interferometric Scattering Microscopy. Annu. Rev. Phys. Chem. 70: 301–322.

18. AL-Khayat, H.A. 2013. Three-dimensional structure of the human myosin thick filament: Clinical implications. Glob. Cardiol. Sci. Pract. 2013: 36.

19. Carlier, M.F. 1991. Actin: protein structure and filament dynamics. J Biol Chem. 266: 1–4.

20. Pardee, J.D., and J.A. Spudich. 1982. Purification of muscle actin. Methods Cell Biol. 24: 271–89.

21. Young, G., N. Hundt, D. Cole, A. Fineberg, J. Andrecka, A. Tyler, A. Olerinyova, A. Ansari, E.G. Marklund, M.P. Collier, S.A. Chandler, O. Tkachenko, J. Allen, M. Crispin, N. Billington, Y. Takagi, J.R. Sellers, C. Eichmann, P. Selenko, L. Frey, R. Riek, M.R. Galpin, W.B. Struwe, J.L.P. Benesch, and P. Kukura. 2017. Quantitative mass imaging of single molecules in solution. bioRxiv. : 229740.

22. Shrivastava, R., D. Köster, S. Kalme, S. Mayor, and M. Neerathilingam. 2015. Tailor-Made Ezrin Actin Binding Domain to Probe Its Interaction with Actin In-Vitro. PLoS One. 10: e0123428.

23. Grover, R., J. Fischer, F.W. Schwarz, W.J. Walter, P. Schwille, and S. Diez. 2016. Transport efficiency of membrane-anchored kinesin-1 motors depends on motor density and diffusivity. Proc. Natl. Acad. Sci. 113: E7185–E7193.

24. Kas, J., H. Strey, and E. Sackmann. 1994. Direct Imaging of Reptation for Semiflexible Actin-Filaments. Nature. 368: 226–229.

25. Smith, D., F. Ziebert, D. Humphrey, C. Duggan, M. Steinbeck, W. Zimmermann, and J. Käs. 2007. Molecular motor-induced instabilities and cross linkers determine biopolymer organization. Biophys. J. 93: 4445–52.

26. Vogel, S.K., Z. Petrasek, F. Heinemann, and P. Schwille. 2013. Myosin motors fragment and compact membrane-bound actin filaments. Elife. 2: 1–18.

27. Baker, J.E., C. Brosseau, P.B. Joel, and D.M. Warshaw. 2002. The biochemical kinetics underlying actin movement generated by one and many skeletal muscle myosin molecules. Biophys. J. 82: 2134–2147.

28. Billington, N., A. Wang, J. Mao, R.S. Adelstein, and J.R. Sellers. 2013. Characterization of three full-length human nonmuscle myosin II paralogs. J. Biol. Chem. 288: 33398–33410.

29. Nedelec, F., and D. Foethke. 2007. Collective Langevin dynamics of flexible cytoskeletal fibers. New J. Phys. 9.

30. Belmonte, J.M., M. Leptin, and F. Nédélec. 2017. A theory that predicts behaviors of disordered cytoskeletal networks. Mol. Syst. Biol. 13: 941.

31. Gittes, F., B. Mickey, J. Nettleton, and J. Howard. 1993. Flexural rigidity of microtubules and actin filaments measured from thermal fluctuations in shape. J. Cell Biol. 120: 923–934.

32. Stam, S., J. Alberts, M.L. Gardel, and E. Munro. 2015. Isoforms confer characteristic force

generation and mechanosensation by myosin II filaments. Biophys. J. 108: 1997–2006.

33. Erdmann, T., and U.S. Schwarz. 2012. Stochastic force generation by small ensembles of myosin II motors. Phys. Rev. Lett. 108: 1–5.

34. Seara, D.S., V. Yadav, I. Linsmeier, A.P. Tabatabai, P.W. Oakes, S.M.A. Tabei, S. Banerjee, and M.P. Murrell. 2018. Entropy production rate is maximized in non-contractile actomyosin. Nat. Commun. 9: 4948.

35. Kovacs, M., K. Thirumurugan, P.J. Knight, and J.R. Sellers. 2007. Load-dependent mechanism of nonmuscle myosin 2. Proc. Natl. Acad. Sci. 104: 9994–9999.

36. Greenberg, M.J., T. Lin, Y.E. Goldman, H. Shuman, and E.M. Ostap. 2012. Myosin IC generates power over a range of loads via a new tension-sensing mechanism. Proc. Natl. Acad. Sci. U. S. A. 109: E2433-40.

37. Alvarado, J., M. Sheinman, A. Sharma, F.C. MacKintosh, and G.H. Koenderink. 2013. Molecular motors robustly drive active gels to a critically connected state. Nat. Phys. 9: 1–7.

38. Ehrlicher, A.J., R. Krishnan, M. Guo, C.M. Bidan, D.A. Weitz, and M.R. Pollak. 2015. Alpha-actinin binding kinetics modulate cellular dynamics and force generation. Proc. Natl. Acad. Sci. 112: 6619–6624.

39. Spudich, J.A., and S. Watt. 1971. The regulation of rabbit skeletal muscle contraction. I. Biochemical studies of the interaction of the tropomyosin-troponin complex with actin and the proteolytic fragments of myosin. J. Biol. Chem. 246: 4866–71.

40. Pollard, T.D. 1982. Myosin purification and characterization. Methods Cell Biol. 24: 333–71.

41. Ortega-Arroyo, J., and P. Kukura. 2012. Interferometric scattering microscopy (iSCAT): new frontiers in ultrafast and ultrasensitive optical microscopy. Phys. Chem. Chem. Phys. 14: 15625.

42. Cole, D., G. Young, A. Weigel, A. Sebesta, and P. Kukura. 2017. Label-Free Single-Molecule Imaging with Numerical-Aperture-Shaped Interferometric Scattering Microscopy. ACS Photonics. 4: 211–216.

43. Li, H., T. Shen, M.B. Smith, I. Fujiwara, D. Vavylonis, and X. Huang. 2009. Automated Actin Filament Segmentation, Tracking, and Tip Elongation Measurements based on Open Active Contour Models. In: In Proc. of the IEEE International Symposium on Biomedical Imaging: From Nano to Macro. Boston: .

44. Smith, M.B., H. Li, T. Shen, X. Huang, E. Yusuf, and D. Vavylonis. 2010. Segmentation and tracking of cytoskeletal filaments using open active contours. Cytoskeleton. 67: 693–705.

45. Meijering, E., M. Jacob, J.-C.F. Sarria, P. Steiner, H. Hirling, and M. Unser. 2004. Design and validation of a tool for neurite tracing and analysis in fluorescence microscopy images. Cytometry. 58A: 167–176.

46. Ortega Arroyo, J., D. Cole, and P. Kukura. 2016. Interferometric scattering microscopy and its combination with single-molecule fluorescence imaging. Nat. Protoc. 11: 617–633.

47. Woody, M.S., J.H. Lewis, M.J. Greenberg, Y.E. Goldman, and E.M. Ostap. 2016. MEMLET: An Easy-to-Use Tool for Data Fitting and Model Comparison Using Maximum-Likelihood Estimation. Biophys. J. 111: 273–282.

Figure 1, experimental setup: **A)** Diagram of the *in-vitro* system consisting of a supported lipid bilayer (orange), actin-membrane linker protein His10-KCK-EzrinABD (HKE; dark grey and red), actin filaments (gray) and muscle myosin II filaments (blue), arrows indicate principle of iSCAT microscopy. **B-C)** Example images of actin filaments (B) and myosin II filaments (C) recorded with a 445 nm laser iSCAT system; scale bar: 2 µm. **D)** Histogram depicting the interferometric contrast distribution along actin filaments (grey, N_{fil}=12, $N_{measure}$=562) and myosin II filaments (blue, N_{fil}=5, $N_{measure}$=96). **E)** Example of tracking a single actin filament (red dashed line, l = 0.4 µm) inside an actin network imaged over 137 s (from dark blue to cyan: 0-137 s); scale bar: 1 µm. **F)** Corresponding mean-squared displacement (MSD) of the filament's center of mass (black) and the components parallel (green) and perpendicular (red) to the actin filament orientation. **G)** Mean-squared displacement of the center of mass of a long actin filament (l= 4 µm, Video 4) (black) and its components parallel (green) and perpendicular (red) to the actin filament orientation, indicating confinement at timescales >10 s. **H)** Box plot comparing the diffusive behavior (characterized by logarithmic slopes of MSD plots) of short (<1.5 um, N = 25) and long (> 1.5 um, N = 14) actin filaments indicating confined diffusion for filaments longer than 1.5 µm due to the surrounding actin meshwork.

Figure 2, myosin II filament dynamics in the acto-myosin network at different ATP concentrations: **A, B)** Histogram of myosin II filament dwell times on actin at t = 1min (100 µM ATP) (N = 6400) (**A**) and at t = 16 min (N = 8000) (B). **C-E)** Histograms of the myosin II filament velocities (**C**), run lengths (**D**) and frequency plot of run length vs dwell time (**E**) extracted from a subset of the myosin II filament kymographs at t = 1min (N=432). **F-H)** Histograms of the myosin II filament velocities (**F**), run lengths (**G**) and frequency plot of run length vs. dwell time (**H**) extracted from a subset of the myosin II filament kymographs at t = 16 min (N=1133). Best fits for the distributions were computed with the MEMLET fitting routine: (A and B), double exponential decay (solid green line, dashed lines indicate 95%

confidence level), (C) double Gaussian (red line), (F) single Gaussian (red line) and (D and G) single exponential decay (black line). Data displayed in (E and H) was limited to binding times of 10 s to focus on details in this dwell time regime.

Figure 3, single particle tracking of myosin II filaments provides further insights into change of myosin dynamics with decreasing ATP concentrations: A, B) Images depicting all tracked myosin II filaments (in alternating colors to distinguish individual tracks) at (**A**) t = 1 min (100 µM ATP)(N = 14016) and (**B**) t = 16 min (N = 15647), scale bar: 5 µm. **C)** Corresponding histogram of myosin II filament dwell times on actin (t = 1 min: green; t = 16 min: purple); best fits for the distributions were computed with the MEMLET fitting routine: triple exponential decay with t_{min} = 0.3s (solid line), boundaries depict 95% confidence level. **D)** Box plot depicting the ratio of processive time versus total dwell time for each processively moving myosin II filament (N(1min) = 221; N(16min) = 640). **E)** Radial histogram depicting the angular difference α between myosin II filament orientation and its velocity vector for all detected myosin II filament steps. **F)** Radial histogram plot depicting the ratio of processive steps versus all detected steps for each angular difference α, indicating that there is a clear increase of filaments that are aligned along their axis of propagation in the contractile state.

Figure 4, dynamics within acto-myosin clusters: **A)** Image sequence depicting the dynamics of myosin II filaments within an acto-myosin cluster; to make the dynamics in the cluster visible, the time median of the image sequence was subtracted from each frame; 635nm iSCAT setup, scale bar 2 µm. **B)** Graph depicting the change of interferometric contrast from the time median of the regions depicted in (**A**) inside (green) and outside (magenta) the cluster. **C)** Snapshots at t = 60 s of simulations of acto-myosin networks using Cytosim with two types of myosin motors with dwell times at τ_1 = 2.4 s (green) and at τ_2 = 10.9 s (red) at ratios indicated in the right top corner mimicking protein concentrations used in

experiments; N(type-1) = 1200, N(motor-2) = [0, 30, 60, 100, 150, 150, 200] from top left to bottom right. **D)** Schematic summarizing the different observed binding modes of myosin II filaments and their assumed effect on the acto-myosin network dynamics and organization.

Table 1, experimental conditions: List of the experimental conditions used in the examples depicted in Figs. 1–5. The table contains the concentration of G-actin, capping protein (CP), myosin II proteins and ATP as well as the average length of actin filaments attached to SLBs, which was measured before the addition of myosin II. Sample size for filament length measurements: N = 505 (Fig.1E-H), N = 151 (Fig 2, 3, 4), N = 255 (Fig S1B), N = 255 (Fig S2A, B).

Figure 1

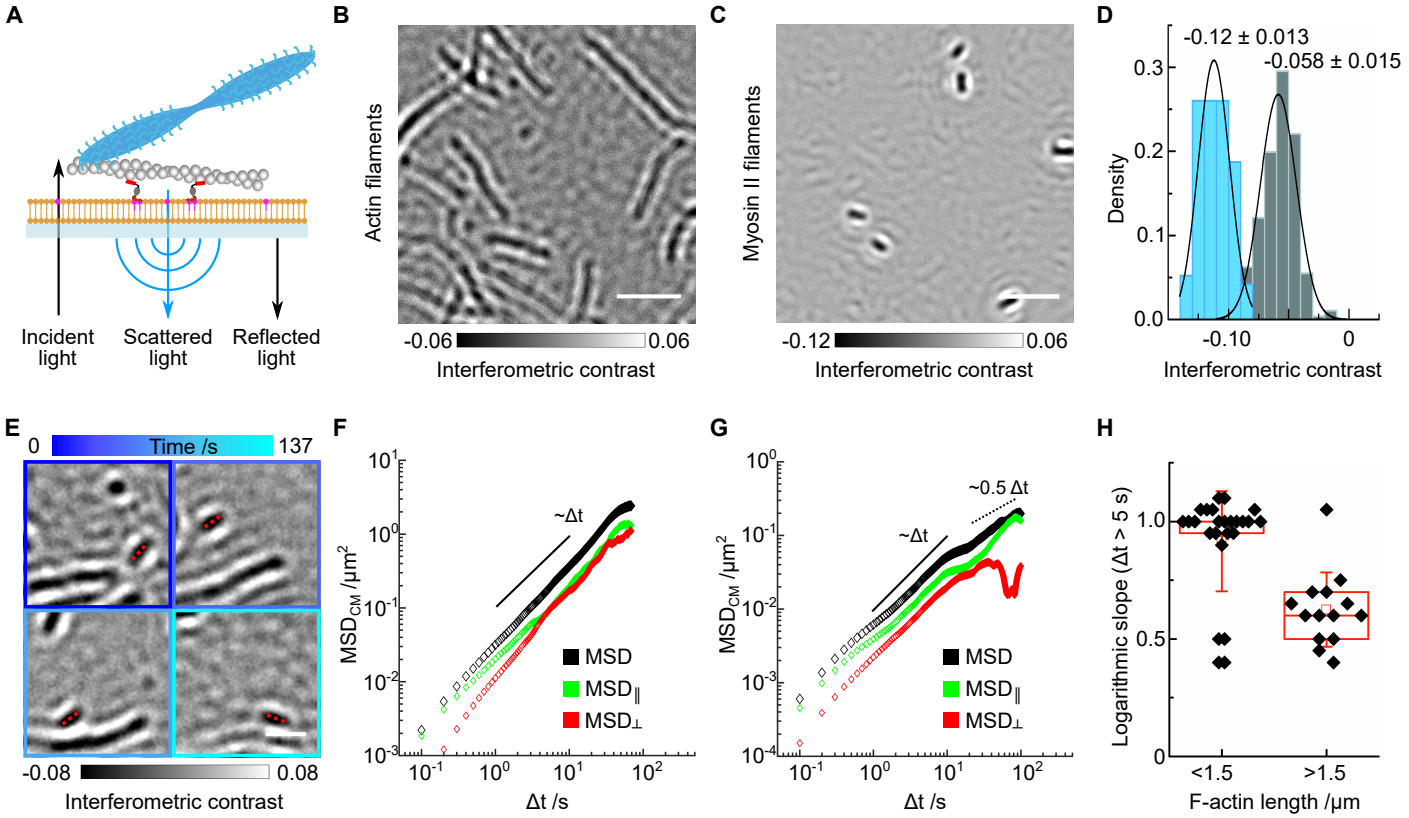
A
Incident light
Scattered light
Reflected light
B
Actin filaments
-0.06
0.06
Interferometric contrast
C
Myosin II filaments
-0.12
0.06
Interferometric contrast
D
-0.12 ± 0.013
-0.058 ± 0.015
Density
0.3
0.2
0.1
0.0
-0.10
0
Interferometric contrast
E
0
Time /s
137
-0.08
0.08
Interferometric contrast
F
~Δt
MSD
MSD∥
MSD⊥
MSDCM /μm2
Δt /s
G
~0.5 Δt
~Δt
MSD
MSD∥
MSD⊥
MSDCM /μm2
Δt /s
H
Logarithmic slope (Δt > 5 s)
1.0
0.5
0
<1.5
>1.5
F-actin length /μm

Figure 2

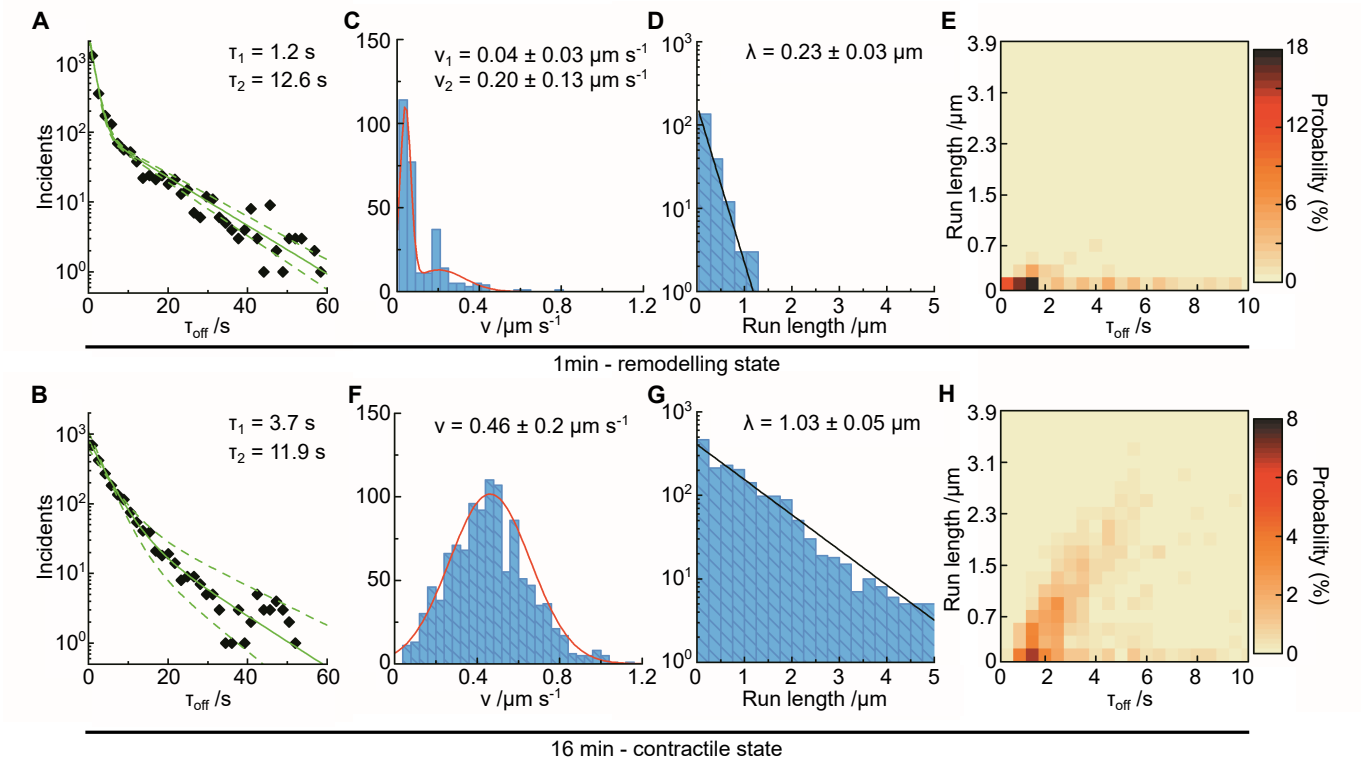
A
τ1 = 1.2 s
τ2 = 12.6 s
Incidents
τoff /s
C
v1 = 0.04 ± 0.03 μm s-1
v2 = 0.20 ± 0.13 μm s-1
v /μm s-1
D
λ = 0.23 ± 0.03 μm
Run length /μm
E
Run length /μm
Probability (%)
τoff /s
1min - remodelling state
B
τ1 = 3.7 s
τ2 = 11.9 s
Incidents
τoff /s
F
v = 0.46 ± 0.2 μm s-1
v /μm s-1
G
λ = 1.03 ± 0.05 μm
Run length /μm
H
Run length /μm
Probability (%)
τoff /s
16 min - contractile state

Figure 3

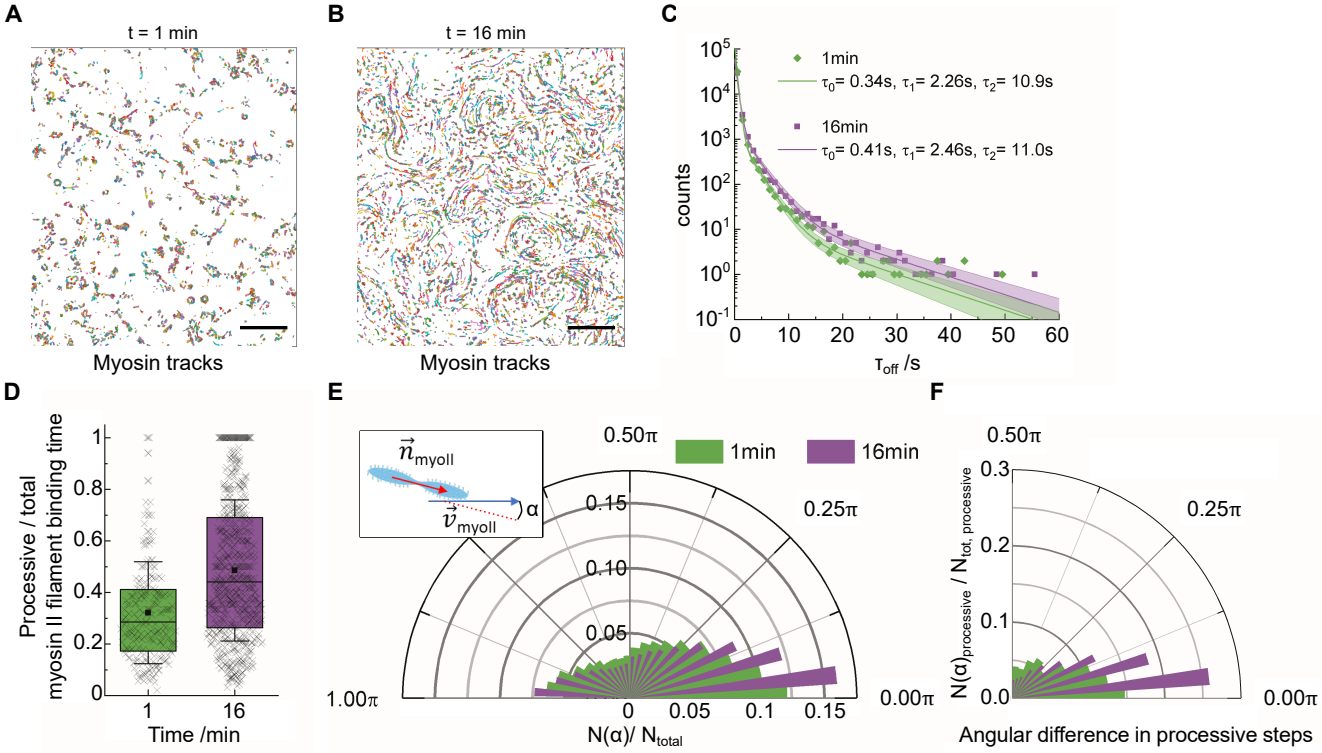
A
t = 1 min
Myosin tracks
B
t = 16 min
Myosin tracks
C
1min
τ0= 0.34s, τ1= 2.26s, τ2= 10.9s
16min
τ0= 0.41s, τ1= 2.46s, τ2= 11.0s
counts
τoff /s
D
Processive / total
myosin II filament binding time
Time /min
E
1min
16min
N(α)/ Ntotal
F
N(α)processive / Ntot, processive
Angular difference in processive steps

Figure 4

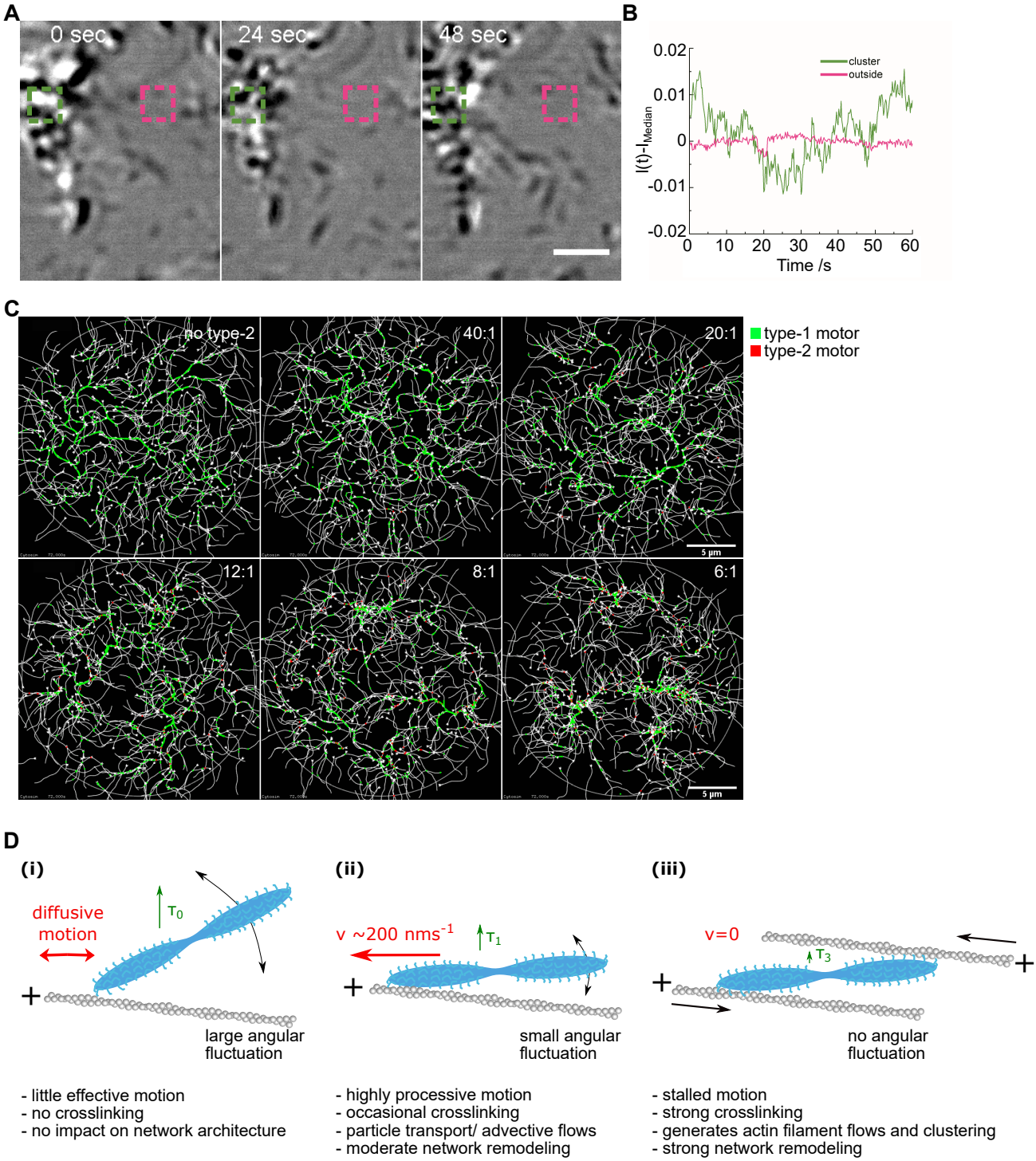

- little effective motion
- no crosslinking
- no impact on network architecture

- highly processive motion
- occasional crosslinking
- particle transport/ advective flows
- moderate network remodeling

- stalled motion
- strong crosslinking
- generates actin filament flows and clustering
- strong network remodeling